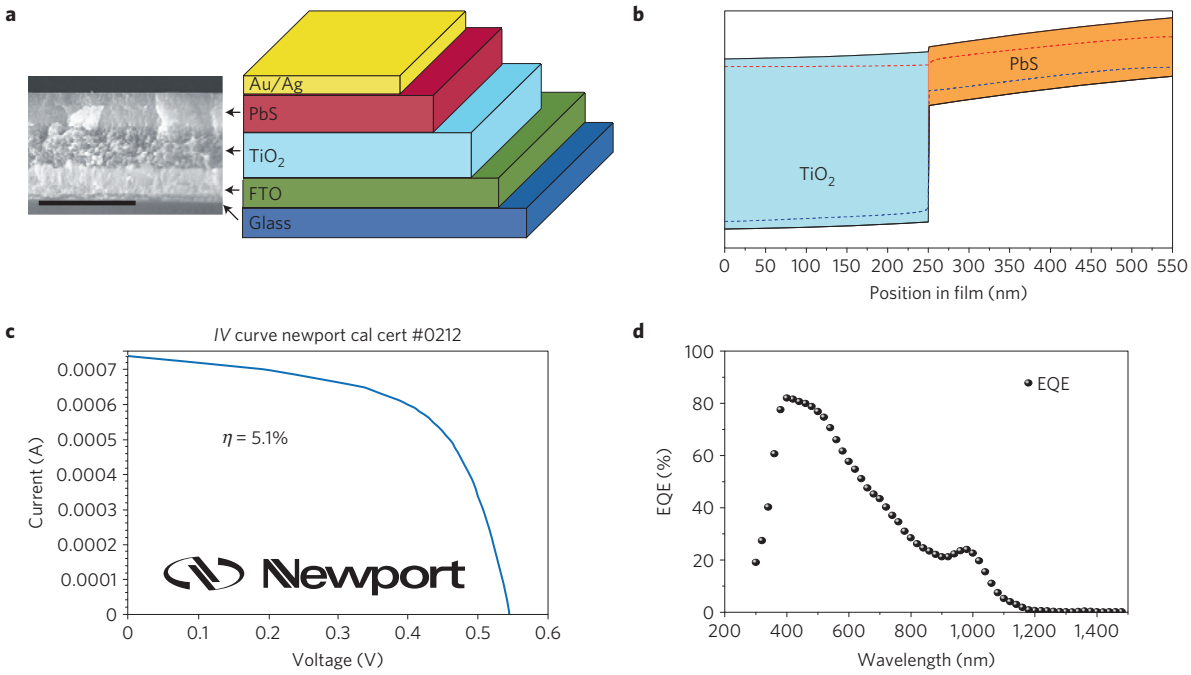


**Figure 3 | Photovoltaic device physics and performance. a**, Schematic of FTO/$TiO_2$/PbS/Au/Ag device architecture. The inset is the cross-sectional SEM images of a representative device. The scale bar is 1 μm. **b**, Band bending of an illuminated $TiO_2$/PbS device under open-circuit conditions. The dashed red and blue lines represent the quasi-Fermi energy of the electrons and holes, respectively. **c**, Device performance measured by a NREL-accredited laboratory (Newport) at 25 °C under 0.93 sun illumination: $V_{oc} = 0.544 \pm 0.006$ V, $I_{sc} = 0.00071 \pm 0.0001$ A, FF = 62 ± 2% and efficiency = 5.1 ± 0.2%. **d**, The white light-biased EQE spectrum of a champion device. The sharp drop in EQE below 400 nm is due to the $TiO_2$ absorption.

films (Fig. 2b). The ~30 meV redshift in optical transitions of the PbS film suggests delocalization of electron and hole wavefunctions due to electronic coupling arising from the reduced interparticle distance (see Supplementary Fig. S3), combined with the effect of the increased dielectric constant[27]. Scanning transmission electron microscopy (STEM) showed that the halide anion treatment resulted—within each sub-layer making up the total multilayer film—in small cracks arising from significant volume contraction when the bulky oleic acid was removed. The analogous effect has been widely observed in CQD films treated with short organic ligands[21,28]. These small cracks were filled by the top layers during the layer-by-layer coating process, leading to the compact and pinhole-free films necessary for photovoltaic device realization (see Supplementary Fig. S4). Grazing-incidence small-angle X-ray scattering (GISAXS) showed no scattering peak in CTAB-treated PbS CQD films, suggesting the absence of in-plane and out-of-plane ordering (see Supplementary Fig. S5), similar to the reduced ordering seen in PbSe CQD film after liquid[27] or vapour[29] phase ethanedithiol (EDT) treatment.

Energy-dispersive X-ray spectroscopy (EDX) and X-ray photoelectron spectroscopy (XPS) analysis (see Supplementary Fig. S6 and Table S2) showed quantitatively significant bromide anion levels in the CTAB-treated PbS CQD film, the quantity consistent with a 1:1 ratio of $Br^-$ to surface $Pb^{2+}$ cations. This 1:1 ratio is reminiscent of the oleate ligand to surface $Pb^{2+}$ concentration in PbSe CQDs seen using NMR (ref. 30). Energy filtered-TEM imaging and elemental mapping were conducted on CTAB-treated samples (see Supplementary Fig. S7). A strong spatial correlation was found between Br, Pb, and S, consistent with bromine present on the quantum dot surface. XPS further indicated a binding energy of Br $3d^{5/2}$ of 68.6 eV (Fig. 2c), in agreement with the binding energy of Br $3d^{5/2}$ in bulk $PbBr_2$ (ref. 31). No other Br chemical state was found in the XPS spectrum. The EDX, energy filtered-TEM, and XPS results confirmed the binding of $Br^-$ to $Pb^{2+}$ on the PbS CQD surface[20].

Minority carrier electron mobility inside our p-type CQD films is a key determinant of overall solar power-conversion efficiency. We employed FET mobility measurements[32] and showed that our halide-terminated films achieved electron mobilities of $4 \times 10^{-2}$ $cm^2$ $V^{-1}$ $s^{-1}$ (see Supplementary Fig. S8). These results, achieved using a room-temperature process, are comparable to those achieved using the hydrazine-based metal–chalcogenide complex route followed by 200 °C annealing[15]. As detailed below, our process provided—compared with organics—an order-of-magnitude enhancement in minority carrier mobility compared with MPA-treated films, and two orders-of-magnitude relative to EDT.

In summary, our atomic-ligand passivation strategy—implemented at room temperature, in air, with no hydrazine, and requiring no annealing—produced an all-inorganic film in which cation-enriched quantum dots were capped with a complete monolayer of halide anions and the mobilities of our films were among the best reported in PbS CQD films[15,32,33].

To build photovoltaic devices, we formed a 270–300 nm thick layer of this inorganic CQD film on a Zr-doped $TiO_2$ electrode residing on fluorine-doped tin oxide (FTO) on glass. The CQD film was ohmically contacted using a sputtered Au top electrode, or equivalently a $MoO_3$/Ag contact. Band bending occurs at the junction between the p-type PbS and n-type $TiO_2$, causing photoelectrons generated in the CQDs to be injected into the $TiO_2$ and collected by the FTO (Fig. 3b). Photogenerated holes travel to the top Au electrode. The cross-sectional SEM micrograph of the $TiO_2$–PbS heterojunction device is included in Fig. 3a.

Device performance was measured by an internationally accredited PV calibration laboratory (Newport Technology and Application Center PV Lab) at 25 °C under 0.93 sun. A certified solar power conversion efficiency of 5.1 ± 0.2% was obtained. An open circuit voltage $V_{oc} = 0.544$ V, short circuit current density $J_{sc} = 14.6$ mA $cm^{-2}$ and fill factor FF = 62% were obtained. This is the first certified CQD solar cell with efficiency >5% (ref. 34) that

**Figure 4 | TRIR characterization of $Br^-$-capped PbS CQD film. a**, Cartoon illustrating the trap-to-band transitions observed in TRIR transient absorption spectra. Bandgap excitation of CQDs results in the formation of excitons from which electrons (holes) can become trapped. Trapped carriers are promoted back into conduction (valence) states through trap-to-band transitions. **b**, The broad features in the TRIR spectra result from trap-to-band transitions observed in PbS CQDs treated with various ligands. The amplitude and shape of the spectra reflect the number and depth of trapped carriers. The narrow features appearing between 0.15 and 0.2 eV correspond to vibrational spectra of ligands that are perturbed by localization of charges at surface trap sites. **c**, The average decay times of the trap-to-band transitions in PbS CQD films are strongly correlated with the average mid-infrared transition energies. **d**, The mobilities of electrons in PbS CQD films are also strongly correlated with the average mid-infrared transition energies for a variety of passivation methods. The $Br^-$-capped PbS CQD film has the highest mobility within the set, consistent with the lower average trap energy as determined by TRIR spectroscopy.

agreed within 0.2 power points with the numbers measured in our own laboratories. Depending on the details of treatment conditions, solar cells showed a $V_{oc}$ ranging between 0.42 and 0.55 V, $J_{sc}$ ranging between 14–24 mA $cm^{-2}$, and FF of 50%–63%. Our measured solar power-conversion efficiencies ranged from 4.8–6.0% (see Supplementary Fig. S9) and a champion device showing static efficiency of 6.0% ($V_{oc} = 0.48$ V, $J_{sc} = 20.2$ mA $cm^{-2}$, FF = 62%) is presented in Supplementary Fig. S10. The corresponding external quantum efficiency (EQE) spectrum is shown in Fig. 3d. The EQE reached 80% in the blue spectral region, consistent with an internal quantum efficiency (IQE) exceeding 90%. Integrating the white light-biased EQE spectrum with the AM1.5G solar spectrum yielded a short circuit current density $J_{sc}$ of 20.4 mA $cm^{-2}$, in good agreement with the measured $J_{sc}$.

$TiO_2$ was measured to have an n-type doping density $N_D$ of $\sim 4 \times 10^{15}$ $cm^{-3}$, in good agreement with literature values for $TiO_2$ processed in air and post-treated with $TiCl_4$; (ref. 35) PbS CQD films were determined from capacitance–voltage measurement to have a p-type doping density $N_A \sim 10^{15}$–$10^{16}$ $cm^{-3}$ (see Supplementary Figs S11–S13). Using the band edge energy measured by cyclic voltammetry[36], we predicted a built-in potential ($V_{bi}$) in our p–n heterojunction device in the range 0.47 ~ 0.53 V, in good agreement with the $V_{bi}$ measured using capacitance–voltage characterization and the device $V_{oc}$ (see Supplementary Figs S14, S15). The measured doping density of the $Br^-$-capped PbS CQD film was one order of magnitude lower than the previously reported MPA- and EDT-treated PbS films. This is consistent with the strong suppression of defect states by our monovalent inorganic passivation strategy.

We therefore sought to investigate the density and energy depth of trap states in the film. Time-resolved infrared (TRIR) spectroscopy[37,38] permits the direct examination of charge traps in quantum dots through excitation of carriers from surface trap states into band states of the quantum dots (see Fig. 4a and Supplementary Fig. S16). Figure 4b presents TRIR spectra measured 500 ns after

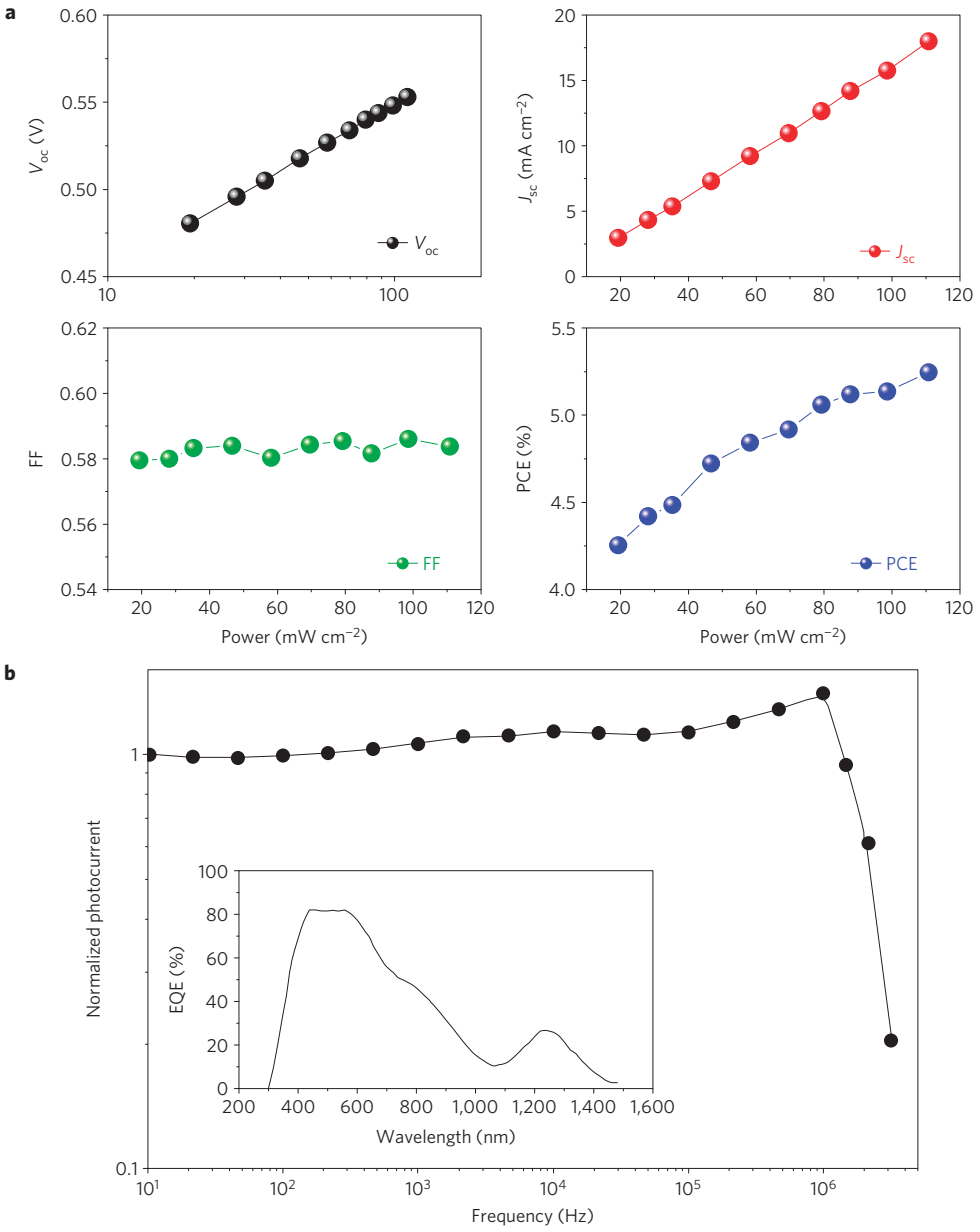


**Figure 5 | Light-intensity-dependent photovoltaic performance and frequency dependent photodiode performance. a**, $Br^-$-passivated CQD photovoltaic devices show a logarithmic increase of $V_{oc}$, a linear increase of $J_{sc}$, a constant FF, and a consequent increase in efficiency as the incident light intensity increases from 0.2 sun to 1.1 sun. The results indicate that passivation is sufficient to maintain acceptably low recombination even at high electron–hole pair generation rates. **b**, Normalized photodiode EQE versus illumination frequency at zero bias. Data were obtained at room temperature using a 640 nm laser diode modulated with a square wave pulse produced by a 20 MHz frequency generator. The inset is the measured wavelength-dependent EQE.

bandgap excitation of PbS CQD solids treated using various organic and inorganic ligands. The spectra are scaled according to the optical absorption of the corresponding CQD films at the excitation wavelength (532 nm) such that the relative signal amplitudes can be compared quantitatively. The spectra contain broad electronic absorption bands arising from excitation of trapped electrons into the band states of the CQD films (see Supplementary Information for detailed assignments). Superimposed on the broad trap-to-band absorption are the narrow vibration features of the ligands that are perturbed by localization of electrons in the surface trap states.

Comparison of the TRIR spectroscopy results with electrical mobility measurements reveals that electrons are trapped in energetically shallower trap states in PbS CQD films capped with $Br^-$ compared with the case of the best organic ligand treatments. The amplitudes of the trap-to-band transitions measured in the TRIR spectra are proportional to the density of trapped carriers at the time of the measurement. Therefore, the lower signal amplitude of the $Br^-$-capped CQD film indicates a lower density of trapped carriers, due in part to the lower trap density and in part to electron and hole recombination. Figure 4c illustrates the average decay time calculated from a multi-exponential fit to normalized TRIR decay curves (inset) measured at the maximum of the corresponding TRIR spectra. The average decay time of the mid-infrared absorption of various CQD solids is strongly correlated with the average trap-to-band transition energy, indicating that $Br^-$-capped PbS CQD solids have on average a smaller trap state energy measured relative to the conduction band. The lower average trap energy from the $Br^-$ treatment also results in higher average mobility, as observed in field-effect mobility measurements (Fig. 4d). The variation of the mobility with the mid-infrared

**Table 1 | Summary of photovoltaic performance of champion devices treated with other inorganic anions.**

| Treated chemicals | Ligands | $J_{sc}$ (mA cm$^{-2}$) | $V_{oc}$ (V) | FF% | PCE% | $R_s$ (Ω cm$^2$) |
|---|---|---|---|---|---|---|
| HTAC | $Cl^-$ | 15.8 | 0.52 | 55 | 4.50 | 5.4 |
| TBAI | $I^-$ | 18.0 | 0.53 | 59 | 5.54 | 4.9 |
| TBAT | $SCN^-$ | 13.6 | 0.52 | 44 | 2.95 | 15.9 |

$Cl^-$-, $I^-$- and $SCN^-$-passivated PbS CQD photovoltaic devices showed power-conversion efficiencies of 4.50%, 5.54% and 2.95%, respectively. $R_s$ is the series resistance.

transition energy indicates that the transition energy is related to the activation energy, $\Delta E$, for charge transport in the CQD solids[33], further supporting the interpretation of the mid-infrared transition in terms of a trap-to-band transition.

The data reveal a 200-fold increase in electron mobility but only a 10-fold decrease in charge recombination lifetime. Our atomic passivation strategy results in a factor of 20 enhancement of the mobility–lifetime product in comparison to EDT passivation, indicating superior charge carrier diffusion in the atomic-ligand-passivated films. The combination of lower trap density, lower trap depth, and higher mobility–lifetime product enables CTAB-treated PbS CQD photovoltaics to achieve unprecedented power-conversion efficiencies.

The good carrier transport in $Br^-$-capped PbS CQD film was also evidenced by the strong suppression of bimolecular recombination. Light-intensity-dependent photovoltaic performance measurement showed a linear correlation between $J_{sc}$ and light intensity, suggesting that no space charge was accumulated because of slow exciton dissociation and carrier transport, even under 1.1 sun illumination[39]. Through the logarithmic increase of $V_{oc}$ and constant FF with increasing light intensity, the devices showed an increased efficiency at higher light intensity (Fig. 5a).

We have made more than 30 nominally identical devices with efficiency above 5.5%. Devices stored in dry ambient for up to 6 days resulted in 1% absolute efficiency loss, associated primarily with loss of $J_{sc}$ and FF (see Supplementary Fig. S17). Ambient oxidation or reaction with moisture may create detrimental defects on PbS CQDs and the $TiO_2$/PbS interface, giving rise to more recombination loss and mobility reduction. Devices stored in a glovebox for three weeks resulted in a 4% relative efficiency loss.

Our atomic-ligand passivation is not limited to $Br^-$-passivated PbS CQD photovoltaics. Photovoltaic devices with the same architecture of FTO/$TiO_2$/PbS/Au, but treated instead with solutions containing salts of $Cl^-$, $I^-$ and $SCN^-$, showed similar performance (Table 1). FET measurement indicated both $Cl^-$ and $I^-$ treatment yield CQD films with electron mobilities exceeding 0.01 cm$^2$ V$^{-1}$ s$^{-1}$, and devices using $I^-$ consistently produce a performance comparable to, and in some cases better than CTAB treatment.

To illustrate the versatility of our atomic ligand strategy, we characterized devices from the perspective of fast photodetection. We adopted a similar device architecture, but used larger PbS CQDs having their absorption peaks at ~1,250 nm. As shown in Fig. 5b, the device showed an EQE reaching 80% in the visible up to 600 nm, proving that $Br^-$ was an effective passivant for much larger CQDs as well. The photodiode showed a 3 dB frequency of 2.4 MHz at room temperature, faster than the previous speed record for PbS CQD photodetectors[40]. We attribute the fast transit time to the high mobility in CTAB-treated PbS CQDs film, leading to a very short drift time in the depletion region. The resultant device provides a record gain–bandwidth product (see Supplementary Fig. S18) for solution-processed photodetectors[1,2,40].

To conclude, we report the first inorganic ligand-passivated CQD photovoltaics. The devices exhibited 6% solar power-conversion efficiency. Our monovalent inorganic ligand passivation strategy enables good passivation of surface defects, high carrier mobility and good device stability, whilst using inexpensive chemicals readily processed in ambient at room temperature. The combined features hold the promise their broad application for other optoelectronic devices based on nanoparticles.

## Methods

Materials preparation: 950 nm and 1,250 nm PbS CQDs are synthesized using a modified recipe described before[17]. $CdCl_2$–TDPA–OLA solution was produced by mixing 2 mM $CdCl_2$ (0.256 g), 0.1 g TDPA and 10 ml OLA in a flask and heating at 100 °C under vacuum for 30 min. $CdCl_2$–TDPA–OLA treatment was carried out using a Schlenk line. For the treatment, 12 ml PbS CQDs solution (50 mg ml$^{-1}$ in octane) and 24 ml toluene were mixed and heated to 60 °C, then 4 ml $CdCl_2$–TDPA–OLA stock solution was injected and kept at 60 °C for 5 min under magnetic stirring. The reaction was terminated by injection of 40 ml acetone and isolated by centrifugation. A further methanol wash was applied to these dots, which were finally dispersed in octane to produce a 50 mg ml$^{-1}$ solution. Such a $CdCl_2$–TDPA–OLA treatment consistently produced 6–18 nm redshift in the excitonic peak of the PbS CQDs.

Photovoltaic Device and Photodiode Fabrication: PbS CQD film was fabricated in ambient atmosphere with low relative moisture (<30%) using a layer-by-layer spin-coating method. 50 mg ml$^{-1}$ Cd-treated PbS CQDs octane solution and 10 mg ml$^{-1}$ CTAB, methanol solution were prepared in advance. All spin-coating steps were at 2,500 r.p.m. Each iteration in the layer-by-layer deposition consisted of three steps: (1) three drops of PbS solution was dropped onto a static $TiO_2$ substrate and spun for 15 s; (2) the film was flushed with 0.25 ml, 0.5 ml or 0.75 ml CTAB methanol solution, left for 1 min and spun (~3 s) to dry the film; the CTAB treatment was repeated another two times; (3) the film was washed by methanol flush and then spun dry three times. We repeated each iteration 6–9 times to obtain a smooth, shiny PbS CQD film. For other halide anion treatments, all fabrication procedures were identical to the CTAB treatment except that 8.8 mg ml$^{-1}$ HTAC, 10.1 mg ml$^{-1}$ TABI or 8.2 mg ml$^{-1}$ tetrabutylammonium thiocyanate (TBAT) methanol solution were used instead. Electrodes were deposited with an Edward 306 evaporator located in ambient environment. 20 nm Au was first deposited by d.c. sputtering (50 W, 0.1 nm s$^{-1}$ under a $N_2$ pressure of $5 \times 10^{-3}$ torr), followed by thermal evaporation of a 100 nm Ag layer (0.5 nm s$^{-1}$ at a pressure of $<1.5 \times 10^{-5}$ torr). A shadow mask was used to define a $4 \times 4$ array of 2.78 mm diameter circular contacts. The active device area is 6.07 mm$^2$. The photodiode was constructed in a similar way to the photovoltaics described above. 1,250 nm PbS quantum dots and 20 mg ml$^{-1}$ CTAB in methanol solution were used to fabricate the 6 LBL film. Molybdenum oxide/silver (15 nm/90 nm) contacts were deposited in an Angstrom Engineering thermal evaporation system. A total active area of 0.049 cm$^2$ was achieved.

Current–voltage ($I$–$V$) data were measured using a Keithley 2400 sourcemeter. The solar spectrum at AM1.5 was simulated to within class A specifications (less than 25% spectral mismatch) with a Xe lamp and filters (Solar Light) and the intensity was adjusted to 100 mW cm$^{-2}$. The source intensity was measured with a Melles–Griot broadband powermeter and a Thorlabs broadband powermeter (responsive from 300 nm to 2,000 nm) through a circular 4.91 mm$^2$ aperture at the position of the sample and confirmed with a calibrated reference solar cell (Newport). The accuracy of the power measurements was estimated to be ±7%. Three strategies were employed in combination to avoid overestimating the power-conversion efficiency: (1) we divided the entire power through the 4.91 mm$^2$ aperture to calculate the efficiency; (2) the spectral mismatch between our simulator spectrum and the reference spectrum ASTM G173-03 was carefully and periodically re-measured; (3) the efficiency variation between different scan rates and between different sweep directions, as well as the maximum power point, was measured to avoid any potential overestimation of efficiency due to hysteresis.

Time-resolved infrared (TRIR) spectroscopy experiments were performed on a home-built instrument consisting of a nanosecond Nd:YAG laser with second harmonic generation (532 nm) as a pulsed laser source to excite the bandgap of the CQD solids. The pulse energy used for the experiments was 150 ± 20 μJ with a corresponding beam diameter of 8 mm, which corresponds to an excitation density of approximately one photon per CQD in the solid film. A compact ceramic Globar Light Source (HORIBA Jobin Yvon) was used to generate the infrared probe. The

continuous wave infrared probe radiation was focused on the sample, overlapped with the laser pulse, and subsequently dispersed in a monochromator (HORIBA Jobin Yvon). Transient absorption measurements were performed by dispersing the probe radiation onto a $1 \times 1$ mm$^2$ MCT (mercury cadmium telluride) single element detector (Infrared Associates) positioned at the focal plane of the monochromator. A preamplifier with band pass frequencies of 1.5 Hz to 1.0 MHz (Infrared Systems Development) was used to amplify the detector signal before digitization with a computer-mounted 1 MHz analog–digital converter card (National Instruments). Throughout the experiment, the monochromator was purged with dry air and the sample stage was raster-scanned using computer-controlled translation stages to prevent photodegradation of the CQD film.

Photodiode characterization was carried out by illuminating the device with a Melles–Griot (56RCS009/HS) 640 nm laser diode, which was modulated using a square wave pulse from a 20 MHz frequency generator (Agilent 33220A). The photocurrent of the device was measured across a resistor placed in series with the device using an Agilent Infiniium Oscilloscope (DSO8104A). A 5 Ω resistor was selected to minimize the effective *RC* constant. The laser response was also measured as a function of frequency, with the amplitude being found to be constant over the range of the experimental measurements.

Received 17 March 2011; accepted 15 August 2011; published online 18 September 2011

## References


1. Konstantatos, G. *et al.* Ultrasensitive solution-cast quantum dot photodetectors. *Nature* **442,** 180–183 (2006).
2. Konstantatos, G., Clifford, J., Levina, L. & Sargent, E. H. Sensitive solution-processed visible-wavelength photodetectors. *Nature Photon.* **1,** 531–534 (2007).
3. Sukhovatkin, V., Hinds, S., Brzozowski, L. & Sargent, E. H. Colloidal quantum-dot photodetectors exploiting multiexciton generation. *Science* **324,** 1542–1544 (2009).
4. Coe, S., Woo, W. K., Bawendi, M. & Bulovic, V. Electroluminescence from single monolayers of nanocrystals in molecular organic devices. *Nature* **420,** 800–803 (2002).
5. Klimov, V. I. *et al.* Optical gain and stimulated emission in nanocrystal quantum dots. *Science* **290,** 314–317 (2000).
6. Tang, J. A. & Sargent, E. H. Infrared colloidal quantum dots for photovoltaics: Fundamentals and recent progress. *Adv. Mater.* **23,** 12–29 (2011).
7. Henry, C. H. Limiting efficiencies of ideal single and multiple energy-gap terrestrial solar-cells. *J. Appl. Phys.* **51,** 4494–4500 (1980).
8. King, R. R. Multijunction cells—record breakers. *Nature Photon.* **2,** 284–286 (2008).
9. Murray, C. B., Kagan, C. R. & Bawendi, M. G. Synthesis and characterization of monodisperse nanocrystals and close-packed nanocrystal assemblies. *Annu. Rev. Mater. Sci.* **30,** 545–610 (2000).
10. Klem, E. J. D. *et al.* Impact of dithiol treatment and air annealing on the conductivity, mobility, and hole density in PbS colloidal quantum dot solids. *Appl. Phys. Lett.* **92,** 212105 (2008).
11. Luther, J. M. *et al.* Schottky solar cells based on colloidal nanocrystal films. *Nano Lett.* **8,** 3488–3492 (2008).
12. Koleilat, G. I. *et al.* Efficient, stable infrared photovoltaics based on solution-cast colloidal quantum dots. *ACS Nano* **2,** 833–840 (2008).
13. Talapin, D. V. & Murray, C. B. PbSe nanocrystal solids for n- and p-channel thin film field-effect transistors. *Science* **310,** 86–89 (2005).
14. Pattantyus-Abraham, A. G. *et al.* Depleted-heterojunction colloidal quantum dot solar cells. *ACS Nano* **4,** 3374–3380 (2010).
15. Kovalenko, M. V., Scheele, M. & Talapin, D. V. Colloidal nanocrystals with molecular metal chalcogenide surface ligands. *Science* **324,** 1417–1420 (2009).
16. Kovalenko, M. V., Bodnarchuk, M. I., Zaumseil, J., Lee, J. S. & Talapin, D. V. Expanding the chemical versatility of colloidal nanocrystals capped with molecular metal chalcogenide ligands. *J. Am. Chem. Soc.* **132,** 10085–10092 (2010).
17. Lee, J. S., Kovalenko, M. V., Huang, J., Chung, D. S. & Talapin, D. V. Band-like transport, high electron mobility and high photoconductivity in all-inorganic nanocrystal arrays. *Nature Nanotech.* **6,** 348–352 (2011).
18. Bryant, G. W. & Jaskolski, W. Surface effects on capped and uncapped nanocrystals. *J. Phys. Chem. B* **109,** 19650–19656 (2005).
19. Gai, Y. Q., Peng, H. W. & Li, J. B. Electronic properties of nonstoichiometric PbSe quantum dots from first principles. *J. Phys. Chem. C* **113,** 21506–21511 (2009).
20. Owen, J. S., Park, J., Trudeau, P. E. & Alivisatos, A. P. Reaction chemistry and ligand exchange at cadmium–selenide nanocrystal surfaces. *J. Am. Chem. Soc.* **130,** 12279–12280 (2008).
21. Tang, J. *et al.* Quantum dot photovoltaics in the extreme quantum confinement regime: The surface-chemical origins of exceptional air- and light-stability. *ACS Nano* **4,** 869–878 (2010).
22. Fernee, M. J. *et al.* Inorganic surface passivation of PbS nanocrystals resulting in strong photoluminescent emission. *Nanotechnology* **14,** 991–997 (2003).
23. Pietryga, J. M. *et al.* Utilizing the lability of lead selenide to produce heterostructured nanocrystals with bright, stable infrared emission. *J. Am. Chem. Soc.* **130,** 4879–4885 (2008).
24. Robinson, R. D. *et al.* Spontaneous superlattice formation in nanorods through partial cation exchange. *Science* **317,** 355–358 (2007).
25. Schapotschnikow, P., Hommersom, B. & Vlugt, T. J. H. Adsorption and binding of ligands to CdSe nanocrystals. *J. Phys. Chem. C* **113,** 12690–12698 (2009).
26. Fritzinger, B., Capek, R. K., Lambert, K., Martins, J. C. & Hens, Z. Utilizing self-exchange to address the binding of carboxylic acid ligands to CdSe quantum dots. *J. Am. Chem. Soc.* **132,** 10195–10201 (2010).
27. Luther, J. M. *et al.* Structural, optical and electrical properties of self-assembled films of PbSe nanocrystals treated with 1,2-ethanedithiol. *ACS Nano* **2,** 271–280 (2008).
28. Zhao, N. *et al.* Colloidal PbS quantum dot solar cells with high fill factor. *ACS Nano* **4,** 3743–3752 (2010).
29. Hanrath, T., Choi, J. J. & Smilgies, D. M. Structure/processing relationships of highly ordered lead salt nanocrystal superlattices. *ACS Nano* **3,** 2975–2988 (2009).
30. Moreels, I., Fritzinger, B., Martins, J. C. & Hens, Z. Surface chemistry of colloidal PbSe nanocrystals. *J. Am. Chem. Soc.* **130,** 15081–15086 (2008).
31. Nefedov, V. I. A comparison of results of an ESCA study of nonconducting solids using spectrometers of different constructions. *J. Electron Spectrosc. Relat. Phenom.* **25,** 29–47 (1982).
32. Kang, M. S., Lee, J., Norris, D. J. & Frisbie, C. D. High carrier densities achieved at low voltages in ambipolar PbSe nanocrystal thin-film transistors. *Nano Lett.* **9,** 3848–3852 (2009).
33. Liu, Y. *et al.* Dependence of carrier mobility on nanocrystal size and ligand length in PbSe nanocrystal solids. *Nano Lett.* **10,** 1960–1969 (2010).
34. Luther, J. M. *et al.* Stability assessment on a 3% bilayer PbS/ZnO quantum dot heterojunction solar cell. *Adv. Mater.* **22,** 3704–3707 (2010).
35. Zaban, A., Meier, A. & Gregg, B. A. Electric potential distribution and short-range screening in nanoporous $TiO_2$ electrodes. *J. Phys. Chem. B* **101,** 7985–7990 (1997).
36. Zhong, H. Z. *et al.* Noninjection gram-scale synthesis of monodisperse pyramidal $CuInS_2$ nanocrystals and their size-dependent properties. *ACS Nano* **4,** 5253–5262 (2010).
37. Zhang, J. & Jiang, X. M. Confinement-dependent below-gap state in PbS quantum dot films probed by continuous-wave photoinduced absorption. *J. Phys. Chem. B* **112,** 9557–9560 (2008).
38. Guyot-Sionnest, P., Shim, M., Matranga, C. & Hines, M. Intraband relaxation in CdSe quantum dots. *Phys. Rev. B* **60,** R2181–R2184 (1999).
39. Riedel, I. *et al.* Effect of temperature and illumination on the electrical characteristics of polymer-fullerene bulk-heterojunction solar cells. *Adv. Funct. Mater.* **14,** 38–44 (2004).
40. Clifford, J. P. *et al.* Fast, sensitive and spectrally tuneable colloidal quantum-dot photodetectors. *Nature Nanotech.* **4,** 40–44 (2009).


## Acknowledgements

This publication is based in part on work supported by Award No. KUS–11–009-21, made by King Abdullah University of Science and Technology (KAUST). We thank Angstrom Engineering and Innovative Technologies for useful discussions concerning material deposition methods and control of the glovebox environment, respectively. The authors thank H. Zhong, R. Li, L. Brzozowski, V. Sukhovatkin, A. Barkhouse, I. Kramer, G. Koleilat, E. Palmiano and R. Wolowiec for their help during the course of study. R.D. acknowledges the financial support of e8 scholarship. K.S.J. and J.B.A. gratefully acknowledge partial support from the Petroleum Research Fund (PRF #49639-ND6), the National Science Foundation (CHE 0846241), and the Office of Naval Research (N00014-11-1-0239).

## Author contributions

J.T. and E.H.S. designed and directed this study and analysed the experimental results. J.T. contributed to all the experimental work. K.W.K. and S.H. carried out the photodiode work and K.W.K. assisted in all the experimental work. K.S.J. and J.B.A. carried out the TRIR experiments and analysed the data. H.L. fabricated the $TiO_2$ electrodes. L.L. synthesized the PbS CQDs. K.W.K., L.L. and R.D. contributed to the solution Cd treatment experiment. D.C, K.W.C. and A.A. carried out the GISAXS and TEM measurements and analysed the data. S.H., M.F., X.W., H.L., A.F. and R.D. assisted in device fabrication and characterization. J.T., J.B.A. and E.H.S. wrote the manuscript. All authors commented on the paper.

## Additional information

The authors declare no competing financial interests. Supplementary information accompanies this paper on www.nature.com/naturematerials. Reprints and permissions information is available online at http://www.nature.com/reprints. Correspondence and requests for materials should be addressed to J.T. or E.H.S.